

IRTF/TEXES Observations of the H II Regions H1 and H2 in the Galactic Centre

Hui Dong^{1,2}, John H. Lacy³, Rainer Schödel¹, Francisco Nogueras-Lara¹, Teresa Gallego-Calvente¹, Jon Mauerhan⁴, Q. Daniel Wang⁵, Angela Coterá⁶, Eulalia Gallego-Cano¹

¹ *Instituto de Astrofísica de Andalucía (CSIC), Glorieta de la Astronomía S/N, E-18008 Granada, Spain*

² *National Optical Astronomy Observatory, Tucson, AZ, 85719, USA*

³ *Department of Astronomy, University of Texas, Austin, TX 78712, USA*

⁴ *Department of Astronomy, University of California, Berkeley, CA, 94720, USA*

⁵ *Department of Astronomy, University of Massachusetts, Amherst, MA, 01003, USA*

⁶ *SETI Institute, Mountain View, CA, 94043, USA*

E-mail: hdong@iaa.es

ABSTRACT

We present new [Ne II] (12.8 μm) IRTF/TEXES observations of the Galactic Center H II regions H1 and H2, which are at a projected distance of ~ 11 pc from the center of the Galaxy. The new observations allow to map the radial velocity distributions of ionized gas. The high spectroscopic resolution (~ 4 km s⁻¹) helps us to disentangle different velocity components and enables us to resolve previous ambiguity regarding the nature of these sources. The spatial distributions of the intensity and radial velocity of the [Ne II] line are mapped. In H1, the intensity distributions of the Paschen- α (1.87 μm) and [Ne II] lines are significantly different, which suggests a strong variation of extinction across the H II region of $A_K \sim 0.56$. The radial velocity distributions across these H II regions are consistent with the predictions of a bow-shock model for H1 and the pressure-driven model for H2. Furthermore, we find a concentration of bright stars in H2. These stars have similar $H-K_s$ colors and can be explained as part of a 2 Myr old stellar cluster. H2 also falls on the orbit of the molecular clouds, suggested to be around Sgr A*. Our new results confirm what we had previously suggested: the O supergiant P114 in H1 is a runaway star, moving towards us through the -30 – 0 km s⁻¹ molecular cloud, whereas the O If star P35 in H2 formed *in-situ*, and may mark the position of a so-far unknown small star cluster formed within the central 30 pc of the Galaxy.

1. Introduction

The Galactic Centre (GC) is the closest galactic nucleus (~ 8.0 kpc, Ghez et al. 2008; Gillessen et al. 2009; Genzel et al. 2010), ~ 100 times closer than the nearest nucleus of another spiral galaxy, the Andromeda galaxy. The GC therefore provides us with a unparalleled template for studying remote galactic nuclei. In addition, understanding star formation within the GC helps in studies of high-redshift galaxies, because their ISM conditions are likely similar (Kruijssen & Longmore 2013).

The collection of giant molecular clouds located within a radius of $\lesssim 200$ pc from the black hole Sgr A* are known as ‘Central Molecular Zone’ (CMZ). This region contains a few times $10^7 M_\odot$ of molecular hydrogen, mostly concentrated in some of the densest clouds in the galaxy (Morris & Serabyn 1996; Launhardt et al. 2002; Ferrière et al. 2007). Even with this huge amount of gas, the star formation rate in the CMZ is an order of magnitude lower than that expected from empirical scaling relations (Longmore et al. 2013). The low star formation rate in the GC is thought to be related to the observed high turbulent pressure (Kruijssen et al. 2014).

Several dynamical models have been developed to explain the spatial and radial velocity distributions of molecular clouds in the GC and how they could collapse to form stars in this extreme environment. Molinari et al. (2011) find that molecular clouds in the GC appear to be aligned along an elliptical, twisted ring. They propose that these clouds could follow a closed elliptical orbit. Kruijssen et al. (2015) propose a different model, with open orbits, which explains why along some lines-of-sight there are three resolved velocity components. They also argue that their model can naturally explain the star formation stages from the ‘Brick’ (no hot protocoresh, Mills et al. 2015, and reference therein) to Sgr B2 (dense star formation regions). During the pericentre passage of Sgr A*, the central massive black hole, these dense clouds are compressed and star formation was triggered. They also claim that two of the three massive star clusters found in the GC, the Arches and Quintuplet clusters (~ 2 and 4 Myr old, Figer et al. 1999, 2002), are aligned with the proposed orbit of the molecular clouds.

Observational evidence confirming this dynamical model is, however, still missing. We have yet to find evidence of star clusters with ages between the Arches (~ 2 - 5 Myr) and Sgr B2 ($\lesssim 1$ Myr), as would be expected based on the model of Kruijssen et al. (2015), and assuming that the molecular clouds in the CMZ continuously pass by Sgr A*. The lack of adequate observational data is mostly due to the fact that the GC is obscured in the ultraviolet and optical bands ($A_V \gtrsim 30$) and the near-infrared (NIR) color similarities of main sequence stars and evolved low-mass stars. We were able to overcome this problem in our *HST*/NICMOS GC survey (Wang et al. 2010; Dong et al. 2011), and succeeded in identifying 100 apparently

isolated candidates of evolved massive stars from their intensity enhancement near $1.87 \mu\text{m}$ due to the Paschen- α and He II lines. Some of these stars are associated with nearby H II regions and may possibly mark so-far unknown young star forming regions. In the follow-up *Gemini* GNIRS/NIFS study of a small sample of eight evolved massive stars near the Arches cluster, Dong et al. (2015) found that P35, an O If star in the H2 H II region, seems to follow the nearby $-30\text{-}0 \text{ km s}^{-1}$ molecular cloud and could have formed *in-situ*. This suggestion was supported by the radial velocity pattern of the ionized gas along the long-slit of *Gemini* GNIRS. However, most of an additional seven nearby stars seem to be interlopers that do not appear to be dynamically related to their associated H II regions. For example, the dynamical pattern of the ionized gas in the nearby H1 H II region ($55''$, i.e. 2.2 pc , away from H2) can be explained by a bow-shock model, which indicates that P114, inside H1, is a runaway star.

In this paper, we complement our previous *Gemini* GNIRS long-slit spectra with new Texas Echelon Cross Echelle Spectrograph (TEXES, Lacy et al. 2002) observations to map the 2-D distribution of the radial velocities of the ionized gas in the H1/H2 regions. We use these data to further study the dynamics of the ionized gas in these two H II regions and how they impact on our understanding of the star formation processes in the CMZ. Our data are described in §2 and the results are presented in §3. We discuss the physical origins of these two H II regions, a new potential star cluster, and how our new results fit into the current concept of the orbit of molecular clouds in the GC in §4. A summary of the work is given in §5.

2. Observations and Data Reduction

2.1. *IRTF*/TEXES observations

We observed the H1 and H2 regions with TEXES on the NASA 3.0 m Infrared Telescope Facility (*IRTF*)¹ on Mauna Kea in April, 2015. TEXES is a high-resolution mid-infrared ($5\text{-}25 \mu\text{m}$) spectrograph. During our observations, TEXES was centered on the [Ne II] ($12.8 \mu\text{m}$) line. Compared to previously used hydrogen recombination lines, [Ne II] suffers less from foreground absorption (for example, $A_{12.8\mu\text{m}} \sim 1.34$, $A_{2.166\mu\text{m}} \sim 2.49$, $A_{1.875\mu\text{m}} \sim 3.55$ toward the GC, from Fritz et al. 2011). Another advantage of using the [Ne II] line is that for gas with $\sim 10^4 \text{ K}$ temperature, velocity broadening introduced by thermal motion in the

¹Infrared Telescope Facility is operated by the University of Hawaii under contract NNH14CK55B with the National Aeronautics and Space Administration.

hydrogen recombination lines is $\sim 21.4 \text{ km s}^{-1}$, but only 4.8 km s^{-1} for the Ne^+ ions, enabling us to more accurately determine the radial velocities of the ionized gas (Zhu et al. 2005).

For our observations, TEXES was operated in high-resolution and mid-resolution modes with resolutions of $\sim 4 \text{ km s}^{-1}$ and $\sim 25 \text{ km s}^{-1}$ along $1.4'' \times 7.5''$ and $1.4'' \times 55''$ slits, respectively. The mid-resolution data completely covers both H II regions, while the high-resolution mode observations missed the southeast corner of H1 (see Fig. 1). The two different resolutions enable us to study the distributions of the intensity and radial velocity, respectively. We scanned the two H II regions using a north-south oriented slit from west to east with a spatial step size of $0.7''$. The integration at each pointing is approximately 15s. An additional 10 pointings before the scientific observations were used to measure the sky background. The spatial resolution was determined by seeing and for these observations is $\sim 1.4''$.

We reduced the data with the standard TEXES pipeline procedure (Lacy et al. 2002). First, we corrected optical distortions, performed flat fielding, applied bad pixel masking, and then removed the cosmic-ray spikes. Second, through measurements of an ambient temperature blackbody before each set of observations, we derived radiometric calibration, which was used to translate the image units from counts to $\text{ergs cm}^{-2} \text{ s}^{-1} \text{ sr}^{-1} (\text{cm}^{-1})^{-1}$. The uncertainty of the measured intensity is mostly systematic and roughly 20%. Third, we used the sky emission lines to calibrate the wavelength, with an accuracy of $\sim 1 \text{ km s}^{-1}$. Fourth, the sky background was subtracted from the observation of each pointing. Finally, multiple pointings were cross-correlated and added to produce the final data cube.

2.2. HST/NICMOS GC Paschen- α Image

The Paschen- α line ($1.87 \mu\text{m}$) image of the H II regions H1 and H2 is from our survey of the GC with the Near-Infrared Camera and Multi-Object Spectrometer (NICMOS) of the Hubble Space Telescope (*HST*). This survey (Wang et al. 2010) mapped the central $36' \times 15'$ of the GC with two narrow-band filters, F187N and F190N. The former band includes both the Paschen- α emission from the H II regions and the stellar continuum at $1.87 \mu\text{m}$, while the latter band just includes the nearby continuum at $1.90 \mu\text{m}$. The pixel size of the final mosaic at these two bands is $0.1''/\text{pixel}$ with a spatial resolution of $0.2''$. Source detection has been performed for individual pointings and filters with ‘Starfinder’ software (Diolaiti et al. 2000), which is then merged into a master catalog. We scaled the F190N mosaic, which was subtracted from the F187N mosaic to get the pure Paschen- α emission. The detailed descriptions of the survey and the data analysis procedures are given in Dong et al. (2011).

2.3. Broad-band photometry from *VLT/HAWKI* survey of the GC

VLT/HAWKI survey of the GC is a large ESO program (Program ID 195.B-0283, PI, Rainer Schödel) and maps the central $46' \times 14'$ field, plus several $8' \times 5'$ fields along and perpendicular to the Galactic Plane, with the J , H and K_s filters, using the *VLT/HAWKI* camera. Its main feature is that this survey uses holographic imaging technique (Schödel et al. 2013), which overcomes the seeing and makes the observations reach a spatial resolution of $0.2''$, similar to our *HST/NICMOS* survey. Due to the broad-band filters used and a bigger collecting area, this *VLT* survey is deeper than the *HST* one. The detailed descriptions of the survey and data reduction procedures are given in Nogueras-Lara et al. (2017, in preparation). For the bright sources, such as P35 and P114, which saturate in the *VLT/HAWKI* survey, we use the photometry from the SIRIUS survey², which has similar filter transmission curves.

3. Results

3.1. Integrated Intensity

Fig 1 shows the Paschen- α image with the contours of integrated [Ne II] line intensity overlaid. The H1 and H2 regions are clearly seen with a size of $\sim 40''$ (1.6 pc) and $15''$ (0.6 pc). The overall structures of the spatial distributions of Paschen- α and [Ne II] line intensities are very similar. H1 shows a cometary structure and is limb-brightened. The peak value of [Ne II] in H1 is $0.07 \text{ ergs cm}^{-2} \text{ s}^{-1} \text{ sr}^{-1}$. The only evolved massive star identified from our previous *HST/NICMOS* GC survey (Dong et al. 2012), P114, an O supergiant, is not located in the center of the cavity. From the projected distance ($5''.5$, i.e. 0.21 pc), P114 is closer to the northern rim of the ionized filaments, which is also the brightest part of this H II region. In contrast, the southwest rim is substantially fainter. The northern rim consists of two parts: the eastern and the western parts; the latter is brighter. On the other hand, H2 represents a fan-like structure. The brightest part of H2 is very close to the central star P35, with a peak value of $0.67 \text{ ergs cm}^{-2} \text{ s}^{-1} \text{ sr}^{-1}$. At the northeastern part the intensity sharply decreases as we move away from the star, while at the southwestern part the intensity decreases slowly. From the morphology of H1 and H2, we roughly infer a -17

²Simultaneous 3-color InfraRed Imager for Unbiased Surveys (SIRIUS) was taken by the Infrared Survey Facility (IRSF) in South Africa, with a pixel scale of $0.45''$ (Nagayama et al. 2003). The survey includes the region $|l| < 2$ degree and $|b| < 1$ degree, with an angular resolution $\sim 1.2''$ in the J band, better than that of 2MASS, $\sim 2''$.

and 20 degree position angles from north to east for the symmetry axes of these two H II regions.

Fig. 2 shows the intensity distributions along several cuts parallel or perpendicular to the symmetry axes of H1 and H2 for both [Ne II] (black solid lines) and Paschen- α (black dotted lines). Considering that the angular resolution of the Paschen- α image is much better than that of the [Ne II] line image (see §2), we convolve the intensity distributions of the Paschen- α image by a Gaussian kernel with a width of $1.4''$. For all the cuts shown in Fig. 2, the peaks of the intensity distribution of the [Ne II] and smoothed Paschen- α match very well. In the cut perpendicular to the symmetry axis of H1, we see the intensity distribution has two distinctive peaks at both wavelengths; with the western peak at an offset of $\sim 5''$ stronger than that at $\sim 3''$. However, the intensity ratio between these two peaks seems to be smaller in the [Ne II] observation. Even if we correct for the spatial resolution differences between the Paschen- α and [Ne II] observations, the difference between these two datasets is still very significant. In order to demonstrate this clearly, in Fig. 3, we show the intensity ratio between the Paschen- α and [Ne II] lines, which as can be seen varies significantly along the cut. The ratio is smallest at offset $\sim 3''$ to $5''$ and is roughly constant away from the brightest part. Extinction, gas excitation and abundance could cause this variation of the intensity ratio. We do not expect any differences in the Ne abundance in this small physical region (< 0.2 pc). Meanwhile, the eastern part (offset $\sim 0''$) of the northern rim is closer to P114 than the western part (offset $\sim 5''$). We also do not find any emission line stars near the western part. Therefore, we do not believe that the small ratio at the western part is caused by higher gas excitation. We suggest that near the brightest Paschen- α peak, the foreground extinction is smaller than that in the neighboring region by $A_{F190N} \sim 0.8$ mag, i.e. $A_K \sim 0.56$ mag and $A_{12.8\mu m} = 0.3$ mag, assuming the extinction curve given in Fritz et al. (2011).

The different extinctions at the two parts are also supported by the colors of nearby stars. Fig.4 presents the color magnitude diagram (CMD, $H-K_s$ vs K_s) of stars found from the VLT/HAWKI survey within $2''$ of the two parts. 10 and 7 out of 18 and 16 detected sources have both H and K_s magnitudes, as well as $H-K_s > 2$, indicating that they are in the GC. The colors of the stars in the western part (‘pluses’) are tighter and bluer than those in the eastern part (‘diamonds’). The difference of the median colors ($H-K_s$) of the stars in these two parts is 0.15 mag, i.e. $A_K \sim 0.21$ mag. The reason why this value is smaller than that derived from the intensity ratio of Paschen- α and [Ne II] lines could be because some stars with higher extinctions are not found in the VLT/HAWKI survey due to the detection limit.

3.2. Velocity Channel Map

Figs 5 and 6 present the velocity channel maps of H1 and H2, respectively, derived from the high-resolution observations. In H1, most of the high velocity Ne II components (-62 km s^{-1} to -50 km s^{-1}) concentrate on the northern part, close to the central star, whereas the intermediate velocity gas (-50 to -30 km s^{-1}) extends to the northwestern part and the low velocity gas (-30 to -10 km s^{-1}) along the ridge, but mostly in the southwestern part. The lower left portion (southeast) of the field covered by the observation completely lacks ionized gas emission. Unlike H1, H2 is bright along the line-of-sight toward P35 over the entire velocity range, indicating that the star is embedded in the ionized gas and its strong stellar wind is pushing surrounding gas away in all directions. The majority of the high velocity gas, is found in the northern part of the H II region. There does not appear to be a consistent gradient of higher to lower velocity gas that is correlated with position.

In Fig. 7, we present the velocity channel maps derived from the mid-resolution observation. Its larger field-of-view and higher sensitivity provide us with more information about the relationship between the two H II regions. Between H1 and H2, there is a weak high-velocity component ($\sim -85 \text{ km s}^{-1}$, $(\delta\text{RA}, \delta\text{Dec})=(25'', -5'')$ relative to P35). South of the H2 region observed in the high resolution observations, there is an ionized ridge with a velocity of $\sim -40 \text{ km s}^{-1}$. Similar ridges have also been seen in the well studied GC H II region, Sgr A-A (Mills et al. 2011). The structure of H1, especially the southern part, which is not covered by the high-resolution observation, is relatively bright at about the same velocity of $\sim -40 \text{ km s}^{-1}$.

3.3. Position-Velocity Diagram

Position-velocity (PV) diagrams along the cuts parallel or perpendicular to the symmetry axes of H1 and H2 are presented in Figs 8–11. In each figure, the cut in the first row passes through the central evolved massive star, P114 or P35.

The velocity field of H1 indicates the presence of an expanding gas bubble around P114. The PV diagrams along the cuts parallel to the symmetry axis (Fig. 8) show that the ionized gas far away from the central star ($13''$ to $20''$ offset, northwest of P114) has -40 km s^{-1} . Closer to P114, two dimmer components become apparent; one with a velocity of -50 km s^{-1} and the other at $\geq -20 \text{ km s}^{-1}$. The two regions are offset $\sim 8''$ from the star along the cut, respectively. The -50 km s^{-1} component appears only to the the east of the symmetry axis (the first and second panels of Fig. 5). The $\geq -20 \text{ km s}^{-1}$ component can be detected in all the three cuts, although it is slightly weaker along the symmetry axis. The PV diagrams along

the cuts perpendicular to the symmetry axis (Fig. 9) show that the high velocity component ($< -40 \text{ km s}^{-1}$) only exists on the eastern (left) part of the northern rim ($\sim 5''$ offset), with the large velocity dispersion is seen at $5''$ and $-10''$ offsets; the radial velocity of the ionized gas, extending from -40 km s^{-1} to -10 km s^{-1} . We do not see a similarly coherent velocity structure at the $-3''$ to $3''$ offsets. Therefore, the shell appears to be incomplete.

In H2, the radial velocity of the ionized gas monotonically decreases from $\sim -60 \text{ km s}^{-1}$ in the head of the H II regions ($\sim 4''$ offset), to -10 km s^{-1} around the central star along cuts parallel to the symmetry axis (Fig. 10). Along the cuts perpendicular to the symmetry axis, there is a large deviation of the radial velocity near the star. We also see a large negative velocity of $\sim -60 \text{ km s}^{-1}$ located $\sim -3''$ to $5''$ from the star along the perpendicular cuts.

4. Discussion

We first compare our results with previous *Gemini*/GNIRS observations in §4.1. Then, we study the physical origins of H1/H2 in §4.2. Third, we discuss the implications of a new star cluster embedded in H2 in §4.3. Finally, we discuss this new star cluster in the context of both the existing dynamical model of molecular clouds and the star formation in this extreme hostile galactic nuclear environment in §4.4.

4.1. Comparison of the *IRTF*/TEXES and *Gemini*/GNIRS observations

Dong et al. (2015) study the radial velocity of ionized gas along a *Gemini*/GNIRS long slit from the $\text{Br}\gamma$ line with a spectral resolution of 40 km s^{-1} in H1 and H2. The spatial positions of the long slit are similar to the cuts parallel to the symmetric axes and passing the central stars given in Figs 8 and 10. In H1, we found the radial velocity of the ionized gas is $-39.6 \pm 2.7 \text{ km s}^{-1}$ at $\sim 6.6''$ and $-72.7 \pm 2.9 \text{ km s}^{-1}$ at $\sim 2.7''$. The former is consistent with the new PV diagram derived from the $[\text{Ne II}]$ line, while we do not detect the latter component in the TEXES dataset, mostly likely due to the low signal-to-noise ratio of our data at that velocity. Conversely, in the *Gemini*/GNIRS dataset, we do not resolve the dim -10 km s^{-1} component seen in the first panel of Fig. 8 due to poor spectral resolution. In H2, Dong et al. (2015) find that the ionized gas peaks at $-63.5 \pm 2.6 \text{ km s}^{-1}$ at $2.9''$ away from the P35, decreasing to $\sim 0 \text{ km s}^{-1}$ near P35. This pattern is fully consistent with the one shown in the first panel of Fig. 10.

4.2. The origins of H1 and H2

Gas kinematics derived from the [Ne II] line play a critical role in enabling us to constrain the underlying physical processes in these H II regions. Different scenarios have been proposed to explain the structures of the H II regions, such as bow shock and pressure driven scenarios. These scenarios could produce similar projected shapes of ionized gas (Zhu et al. 2008). Consequently, the morphology alone is not enough to distinguish which of these scenarios is correct. The two models, however, predict different radial velocities for ionized gas as related to nearby neutral gas.

Dong et al. (2015) find that the ‘bow shock’ and ‘pressure-driven’ scenarios are able to explain the one-dimensional radial velocities of the ionized gas in H1 and H2, respectively. In the case of H1, a massive star is quickly moving into an existing molecular cloud. Its strong stellar wind compresses the surface of the molecular cloud and produces a thin shell. In the case of H2, the star with the stellar wind is at rest relative to the nearby molecular cloud. This results in a fan-like H II region due to the density gradient of the molecular cloud; the stellar wind breaks up the molecular cloud starting from the low density region and moves towards us, while the bright part of the H II region represents higher densities. Dong et al. (2015) reach the above conclusion from only one-dimension measurements of the radial velocity of the ionized gas. Here, we further test the scenarios with new *IRTF*/TEXES data.

For H1, Dong et al. (2015) argue that P114 is behind the molecular cloud and is moving towards us with an angle of inclination between 0 and 90 degree. Each line-of-sight includes the emission from the front and back sides of the thin shell produced by the stellar wind. Ionized gas from the thin shell produced by the stellar wind is blueshifted relative to nearby neutral gas (~ -30 to -40 km s⁻¹, according to Fig 9 in Henshaw et al. 2016). This effect becomes increasingly apparent toward the central star. The velocity becomes more negative when moving closer to P114 in the PV diagram of Fig. 8 in Dong et al. (2015) (-72.7 km s⁻¹ component). A similar effect can be seen in the northern part of the H1 region along the cuts parallel to the symmetry axis shown in Fig. 8. The -40 km s⁻¹ component behind the thin shell ($15''$ offset in Fig. 8) traces the velocity of the molecular cloud. When moving towards P114, the components with velocities smaller and bigger than -40 km s⁻¹ are from the front and back sides of the thin shell. In the latter case, the ionized gas is far and moves away from P114, although with a absolute velocity that is rather small. The same large range of the radial velocities is seen in the cut perpendicular to the symmetry axis and passing from the brightest part of the shell (the bottom panel of Fig. 9), which should trace the emission from the two sides of the shell. The southern part of H1, which is far away from P114, could be the photo-ionized surface of the nearby molecular cloud, a result of the ultraviolet photons from the O supergiant P114. Therefore, the velocity derived from [Ne II] line is

similar to that of nearby molecular clouds. On the other hand, in a pressure-driven model, all the ionized gas moves towards us following the surface of the shell and no radial velocities bigger than -40 km s^{-1} are expected in the PV diagram shown in Fig. 8 and Fig. 9.

One major concern in the bow shock interpretation of H1 in Dong et al. (2015) is correctly interpreting the foreground extinction toward P114 and its effect on the observed Paschen- α emission, since the scenario expects extra extinction from the foreground molecular cloud. One potential solution is that P114 has already reached the front side of the molecular cloud. This is supported by the fact that the western part of the northern rim in H1 shows ~ 0.6 mag at K_s (or ~ 0.3 mag at $12.8 \mu\text{m}$) less extinction than seen in the eastern part. If the molecular cloud in the western part of the northern rim was possibly already destroyed, this also explains why no large negative velocities are seen there (offset -10'), but are only found at $\sim 5\text{'}$ (see the last panel of Fig. 9). Although the western part is further away from P114 than the eastern part in projected distance, the [Ne II] line emission suffers from less foreground extinction by a factor of 1.3 in the western part, which explains why the brightest peak falls in the western part, but not the eastern part. Such a spatial variation of extinction is not expected by the pressure-driven model, in which we directly see the inner surface of molecular cloud facing the central star.

On the other hand, the PV diagrams of H2 in Figs. 10 and 11 are fully consistent with predictions of the pressure driven model. For the cuts parallel to the symmetric axis, near the star, the ionized gas has the lowest velocity relative to nearby neutral gas. When moving away from the apex of the paraboloid, the ionized gas has been accelerated due to the pressure gradient. For the cuts perpendicular to the symmetric axes, both sides of P35 collect the emission from ionized gas along the front and back sides of the paraboloid and therefore show large velocities spanning a large range, most of which are blueshifted relative to the nearby neutral gas (Fig. 11).

In summary, our *IRTF*/TEXES data show more detailed velocity structures in the two H II regions, and provide further evidence that the scenarios proposed in Dong et al. (2015) are correct.

4.3. A new star cluster in the central $10'$ of the GC?

If H2 indeed is the natal cloud of P35, one would then wonder whether or not P35 has formed alone or, as is more likely, is part of a cluster. We therefore examine in detail the existing near-IR photometry data to study the stellar number density distribution and the CMD of the stars near P35.

Fig 12 compares the spatial distribution of stars with F190N magnitudes greater than 11, 12, 13 and 14 from our *HST*/NICMOS survey³. Those dimmer than 14 mag should mostly be Red Clump stars (Figure 14 in Dong et al. 2011). Although it is difficult to see a clear concentration of stars brighter than 12 mag due to the small stellar number density, we can see an enhancement of stellar number density near the H2 for stars with F190N < 13 mag, but not in H1. These stars are distributed mostly in the direction away from the -30-0 km s⁻¹ molecular cloud, which is in the north of H1 and H2. In order to further quantitatively demonstrate this enhancement, we smoothed the stellar number density map for stars with F190N < 13 mag by a Gaussian kernel with a full width half maxim of 20". The stellar number densities in H1 and H2 are 0.017 and 0.022 arcsec⁻², which are 1.7 and 3 sigma above the mean value in the field-of-view of Fig.1. This confirms that there are more stars near H2. We examined the extinction map (A_{F190N}) given in Dong et al. (2011) to explore the possibility whether the number density fluctuation is introduced by the spatial variation of the extinction. In our field-of-view, the median and 68% of the extinction, A_{F190N} , is 3.11 mag and 0.27 mag. On the other hand, the A_{F190N} within 10" of H2 and P35, A_{F190N} are 3.07 ± 0.36 and 3.2 mag (derived from the *J-K* color in Dong et al. 2012), which is not systematically lower than the average value of the whole field-of-view. Therefore, we conclude that the spatial variation of extinction is not responsible for the higher stellar number density in H2.

In Fig. 13, we plot the *H-K_s* vs. *K_s* CMD of the stars within the central 20" of H2. Unfortunately, most of the stars (76%) do not have available *J* band magnitudes; *J-K_s* would allow for a better stellar population analysis. Six of the 12 stars with available F190N magnitude within the central 10" of H2 have similar *H-K_s* colors. Dong et al. (2015) estimate the age of P35 to be roughly 2 Myr. Therefore, we overlay a Geneva stellar isochrone (Ekström et al. 2012) with solar metallicity and an age of 2 Myr on the CMD of Fig. 13. The distance modulus (8 kpc) and the foreground extinction derived from the color of P35 ($A_{K_s}=2.45$, Dong et al. 2012) are included in the calculation of the isochrone. The six stars are indeed very close to the 2 Myr old isochrone, and are certainly bluer than the similar isochrone of an age 5 Gyr. This result should be robust because of the small color uncertainty of these bright stars. If they were evolved low-mass stars, their colors would suggest an extinction $A_{K_s}=0.3$ mag less than that derived for P35. Such a decreased extinction would not be consistent with the nearly constant ratio of the [Ne II] and Paschen- α intensities across H2. Therefore, it is unlikely that these stars are evolved low-mass stars that have similar colors due to lower extinction.

³We do not use the *VLT*/HAWKI observation at the *K_s* band here, because bright stars saturate.

4.4. The impact on the star formation in the GC

How would our new star cluster fit into the big picture of the star formation process in the GC?

Recently, Steinke et al. (2016) reports a new cluster in the Sickle Nebula, which includes one WN6 star (WR102c), one O7? star and three B stars. The WN6 star and the other four early-type stars have similar radial velocities, which suggests that they could be bound in a cluster of total stellar mass $\sim 1000 M_{\odot}$. Because this cluster is close to the Quintuplet cluster ($\sim 50''$, 2 pc), they may be related to the same starburst activity.

Similarly, our cluster also has only one evolved star, P35, an O If star, which will eventually become a WN star (Crowther 2007). Therefore, it is not surprising that the star would be associated with a possible cluster with a similar total stellar mass to the new cluster in the Sickle Nebula. However, the H2 cluster is far away from any other known ones, especially the three known massive clusters (e.g. P35 is $\sim 7.5'$ and $5'$, i.e. 18 pc and 12 pc, in projected distances away from the Arches and Central clusters). Therefore, P35 represents a small cluster with at least one massive star formed in relative isolation.

Dong et al. (2015) suggest that the star formation processes in H2 could have been triggered when the $-30-0 \text{ km s}^{-1}$ molecular cloud passed near Sgr A* (Longmore et al. 2013) about 2-2.5 Myr ago. According to this scenario, at this point, H2 would be on the back side of the orbit proposed by Molinari et al. (2011), assuming a period of ~ 3 Myr. Since Molinari et al. (2011), a new orbit for the molecular clouds has been proposed by Kruijssen et al. (2015), which is overlaid on the *Spitzer*/IRAC 8.0 μm image (Stolovy et al. 2006) and *HST*/NICMOS Paschen- α image in Fig. 14. The green and cyan parts of the orbit are in the front side, while the red portion is the back side. In this model, H2 falls on the front orbital side (green line) and is about 0.1 Myr beyond the point of pericentre passage. For comparison, the well known ‘Brick’ passed the pericentre point ~ 0.3 Myr ago. This is apparently inconsistent with P35 having evolved to an O If star. It thus seems that H2 is in conflict with the star formation sequence between the ‘Brick’ and Sgr B2. We consider two alternative possibilities: 1) H2 is not on the front side of the orbits (green line), but the back side (red line). The green and red parts of the orbit intersect near H2 in the projection. They have similar radial velocities (Figure 4 in Kruijssen et al. 2015). Therefore, it is possible that P35 is associated with the molecular cloud on the back side of the orbit, which passed by Sgr A* about 1.6 Myr ago. 2) The formation of the H2 cluster was triggered in an even earlier pericentre passage, i.e. 2.1 Myr ago (see Figure 6 of Kruijssen et al. 2015).

Besides H2, several well-known H II regions, as well as newly discovered ones (Wang et al. 2010), fall onto the orbit of molecular clouds and could represent the star formation

induced by their pericentre passages. First, we consider H3, H4, H6 and H7, among the eight H II regions (H 1-8) identified by Yusef-Zadeh & Morris (1987) in the region between the Arches cluster and Sgr A*. Dong et al. (2015) show the presence of single evolved massive star in each center of H5 and H8. They find that the radial velocities of these stars are significantly different from those of nearby ionized and neutral gas. This indicates that the stars are likely interlopers and did not form *in-situ*. In the other four H II regions, H3, H4, H6 and H7, no evolved massive stars have been found, although the possibility exists that there are still embedded massive main-sequence stars in these H II regions. The massive main-sequence stars normally have hydrogen or helium absorption lines. Therefore, they cannot be identified by their Paschen- α emission lines in the work by Dong et al. (2012). Another possibility is that the hydrogen emission lines from the central evolved massive stars are diluted by the emission from the surrounding dust, like the dusty WC stars (Dong et al. 2012). Furthermore, H6 and H7 with size of ~ 0.1 pc could be ultracompact H II regions. Compared to H2, the embedded stars could be less massive and therefore do not have enough ionization luminosities nor have they had time to disperse the surrounding dense molecular gas. Second, let us consider several new H II regions identified by our *HST*/NICMOS Paschen- α survey in the region Galactic West to Sgr A* (see the circles, ellipse and boxes in the bottom panel of Fig. 14). The detailed Paschen- α image of the H II region enclosed by the ellipse can be found in Figure 3 of Wang et al. (2010). All of these regions contain evolved massive stars, such as WN, Ofpe/WN9, WC9d, B supergiant, and their candidates (Muno et al. 2006; Cotera et al. 1999; Mauerhan et al. 2010a,b; Dong et al. 2012). Some of them are close to the molecular cloud orbit, which include those marked by the ellipse and the two circles. Therefore, they may be molecular clouds that have experienced star formation induced by the pericentre passage around Sgr A*. The two regions marked by the boxes are somewhat off the orbit and may have different origins. In conclusion, we have demonstrated that star clusters associated with the H II regions, aided by the CMD analysis could help us constrain their ages and the star formation history in the GC.

5. Summary

In this work, we have mapped the radial velocity distribution of ionized gas in two H II regions in the GC, H1 and H2, using our new *IRTF*/TEXES observations of the [Ne II] 12.8 μm line. We have also examined the spatial distribution and color magnitude diagram of an apparent stellar concentration in and around H2. We summarize our results below:

- The [Ne II] emission morphologically follows the Paschen- α emission well, indicating both are from the ionized gas produced by massive stars at the surface of adjacent

molecular clouds.

- The intensity ratio between Paschen- α and [Ne II] line near the bright Paschen- α region in H1 is larger than that in the surrounding region, indicating a local extinction drop of ~ 0.56 mag in the K_s band.
- The velocity structures of H1 and H2 can be well explained by the bow-shock and pressure driven models, respectively.
- The stellar concentration around H2 shows a color magnitude diagram that is consistent with the presence of a 2 Myr old stellar cluster, as hypothesized previously (Dong et al. 2015).
- The location of H2 on the orbit of a molecular cloud chain, as proposed by Kruijssen et al. (2015), which indicates that the formation of this cluster may be triggered by a close passage of its parent cloud around Sgr A* ~ 2 Myr ago.

Acknowledgments

We thank the anonymous referee for a thorough, detailed, and constructive commentary on our manuscript. The research leading to these results has received funding from the European Research Council under the European Union’s Seventh Framework Programme (FP7/2007-2013) / ERC grant agreement n [614922]. F N-L acknowledges financial support from a MECD predoctoral contract, code FPU14/01700. This work uses observations made with the NASA/ESA Hubble Space Telescope and the data archive at the Space Telescope Science Institute, which is operated by the Association of Universities for Research in Astronomy, Inc. under NASA contract NAS 5-26555. This work is also based on observations collected at the European Organisation for Astronomical Research in the Southern Hemisphere under ESO programme(s) 195.B-0283(A).

REFERENCES

- Cotera, A. S., Simpson, J. P., Erickson, E. F., et al. 1999, ApJ, 510, 747
- Crowther, P. A. 2007, ARA&A, 45, 177
- Diolaiti, E., Bendinelli, O., Bonaccini, D., Close, L., Currie, D., Parmeggiani, G., 2000, A&AS, 147, 335

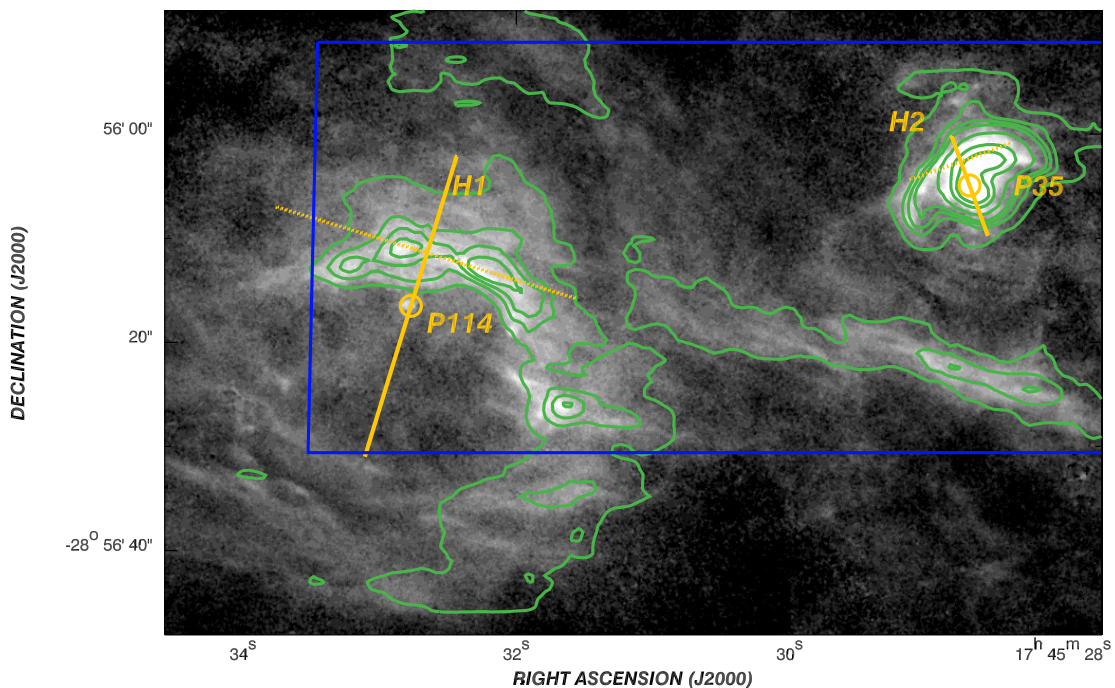


Fig. 1.— The contour lines outline the intensity of the [Ne II] ($12.8 \mu\text{m}$) line overlaid on the *HST*/NICMOS Paschen- α image of the H1 and H2 regions. The contour levels are at 5%, 8%, 10%, 12%, 20%, 40% and 60% of the peak intensity, $0.67 \text{ erg s}^{-1} \text{ cm}^{-2} \text{ sr}^{-1}$. The blue box outlines the area mapped in the high-resolution mode. The yellow circles mark the two evolved massive stars, P114 and P35, associated with the H1/H2 H II regions (Dong et al. 2015). The yellow solid lines represent our proposed (approximately) symmetry axes of these two H II regions, while the dashed lines show the perpendicular directions. The intensity distributions along these lines are presented in Fig. 2.

Dong, H., Wang, Q. D., Cotera, A., et al. 2011, *MNRAS*, 417, 114

Dong, H., Wang, Q. D., & Morris, M. R. 2012, *MNRAS*, 425, 884

Dong, H., Mauerhan, J., Morris, M. R., Wang, Q. D., & Cotera, A. 2015, *MNRAS*, 446, 842

Ekström, S., Georgy, C., Eggenberger, P., et al. 2012, *A&A*, 537, A146

- Ferrière, K., Gillard, W., & Jean, P. 2007, *A&A*, 467, 611
- Figer, D. F., McLean, I. S., & Morris, M. 1999, *ApJ*, 514, 202
- Figer, D. F., Najarro, F., Gilmore, D., et al. 2002, *ApJ*, 581, 258
- Fritz, T. K., Gillessen, S., Dodds-Eden, K., et al. 2011, *ApJ*, 737, 73
- Genzel, R., Eisenhauer, F., & Gillessen, S. 2010, *Reviews of Modern Physics*, 82, 3121
- Ghez, A. M., Salim, S., Weinberg, N. N., et al. 2008, *ApJ*, 689, 1044
- Gillessen, S., Eisenhauer, F., Trippe, S., et al. 2009, *ApJ*, 692, 1075
- Henshaw, J. D., Longmore, S. N., Kruijssen, J. M. D., et al. 2016, *MNRAS*, 457, 2675
- Kruijssen, J. M. D., & Longmore, S. N. 2013, *MNRAS*, 435, 2598
- Kruijssen, J. M. D., Longmore, S. N., Elmegreen, B. G., et al. 2014, *MNRAS*, 440, 3370
- Kruijssen, J. M. D., Dale, J. E., & Longmore, S. N. 2015, *MNRAS*, 447, 1059
- Lacy, J. H., Richter, M. J., Greathouse, T. K., Jaffe, D. T., & Zhu, Q. 2002, *PASP*, 114, 153
- Launhardt, R., Zylka, R., & Mezger, P. G. 2002, *A&A*, 384, 112
- Longmore, S. N., Bally, J., Testi, L., et al. 2013, *MNRAS*, 429, 987
- Mauerhan, J. C., Muno, M. P., Morris, M. R., Stolovy, S. R., & Cotera, A. 2010a, *ApJ*, 710, 706
- Mauerhan, J. C., Cotera, A., Dong, H., Morris, M. R., Wang, Q. D., Stolovy, S. R., & Lang, C. 2010c, *ApJ*, 725, 188
- Mills, E., Morris, M. R., Lang, C. C., et al. 2011, *ApJ*, 735, 84
- Mills, E. A. C., Butterfield, N., Ludovici, D. A., et al. 2015, *ApJ*, 805, 72
- Molinari, S., Bally, J., Noriega-Crespo, A., et al. 2011, *ApJ*, 735, L33
- Morris, M., & Serabyn, E. 1996, *ARA&A*, 34, 645
- Muno, M. P., Bower, G. C., Burgasser, A. J., Baganoff, F. K., Morris, M. R., Brandt, W. N., 2006, *ApJ*, 638, 183M

- Nagayama, T., Nagashima, C., Nakajima, Y., Nagata, T., Sato, S., Nakaya, H., Yamamuro, T., Sugitani, K., Tamura, M., 2003, SPIE, 4841, 459N
- Schödel, R., Yelda, S., Ghez, A., et al. 2013, MNRAS, 429, 1367
- Steinke, M., Oskinova, L. M., Hamann, W.-R., et al. 2016, A&A, 588, A9
- Stolovy, S., Ramirez, S., Arendt, R. G., et al. 2006, Journal of Physics Conference Series, 54, 176
- Wang, Q. D., Dong, H., Cotera, A., et al. 2010, MNRAS, 402, 895
- Yusef-Zadeh, F., Morris, M., 1987, ApJ, 320, 545
- Zhu, Q., Lacy, J. H., & Jaffe, D. T. 2005, Bulletin of the American Astronomical Society, 37, 81.18
- Zhu, Q.-F., Lacy, J. H., Jaffe, D. T., Richter, M. J., & Greathouse, T. K. 2008, ApJS, 177, 584

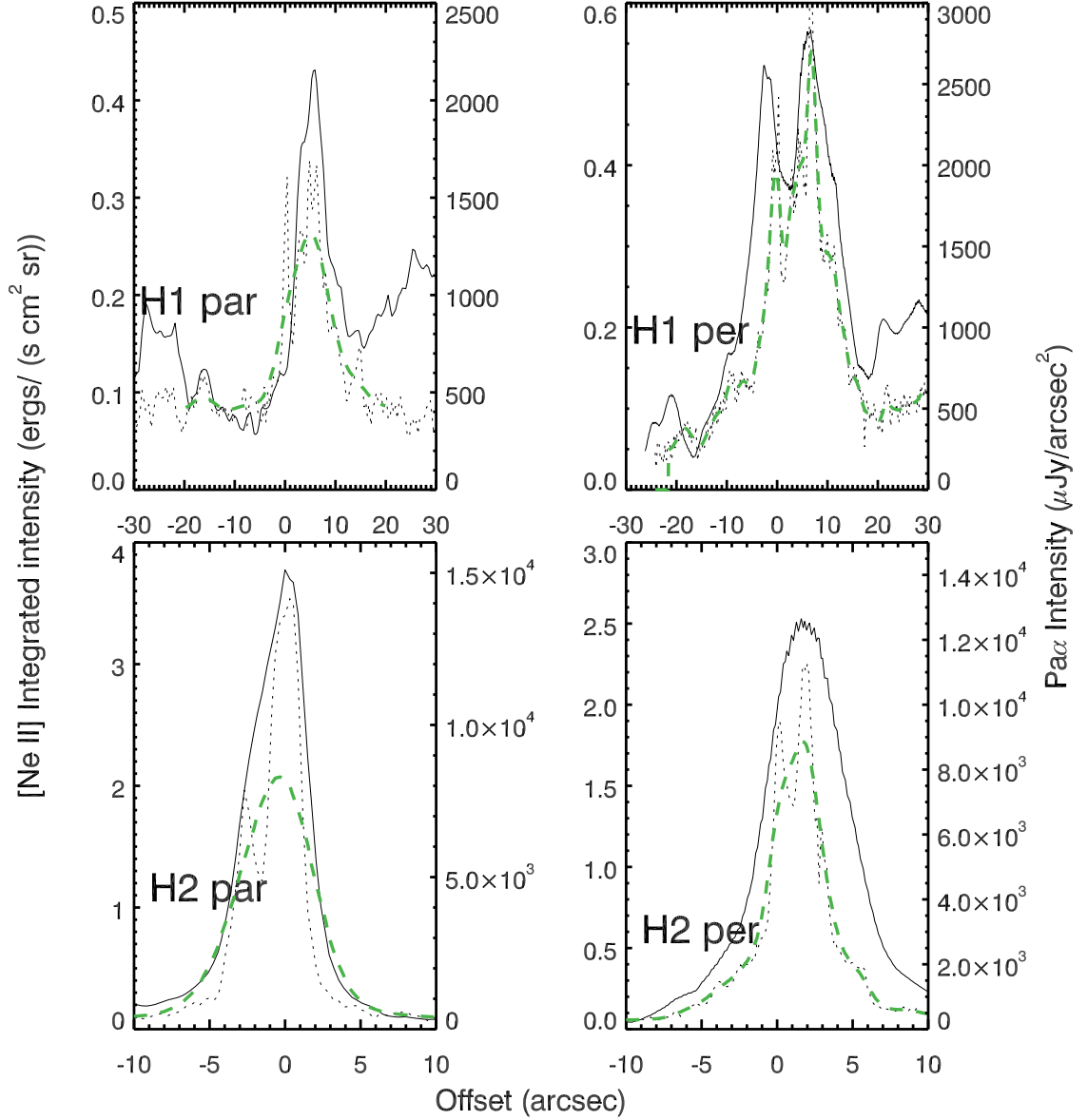


Fig. 2.— Integrated intensity distributions along the yellow solid (left panels) and dashed (right panels) lines in Fig 1 of the H1 (top panels) and H2 (bottom panels). The zero offsets in the left panels are at P114 and P35, respectively, while those in the right panels are at the interactions of the yellow solid and dashed lines in Fig 1. The solid curves are for the [Ne II] line, while the dotted curves are for the Paschen- α line. The green dashed curves represent the intensity distributions of Paschen- α line convolved with a Gaussian kernel of $1.4''$ to match the resolution of the [NeII] observations.

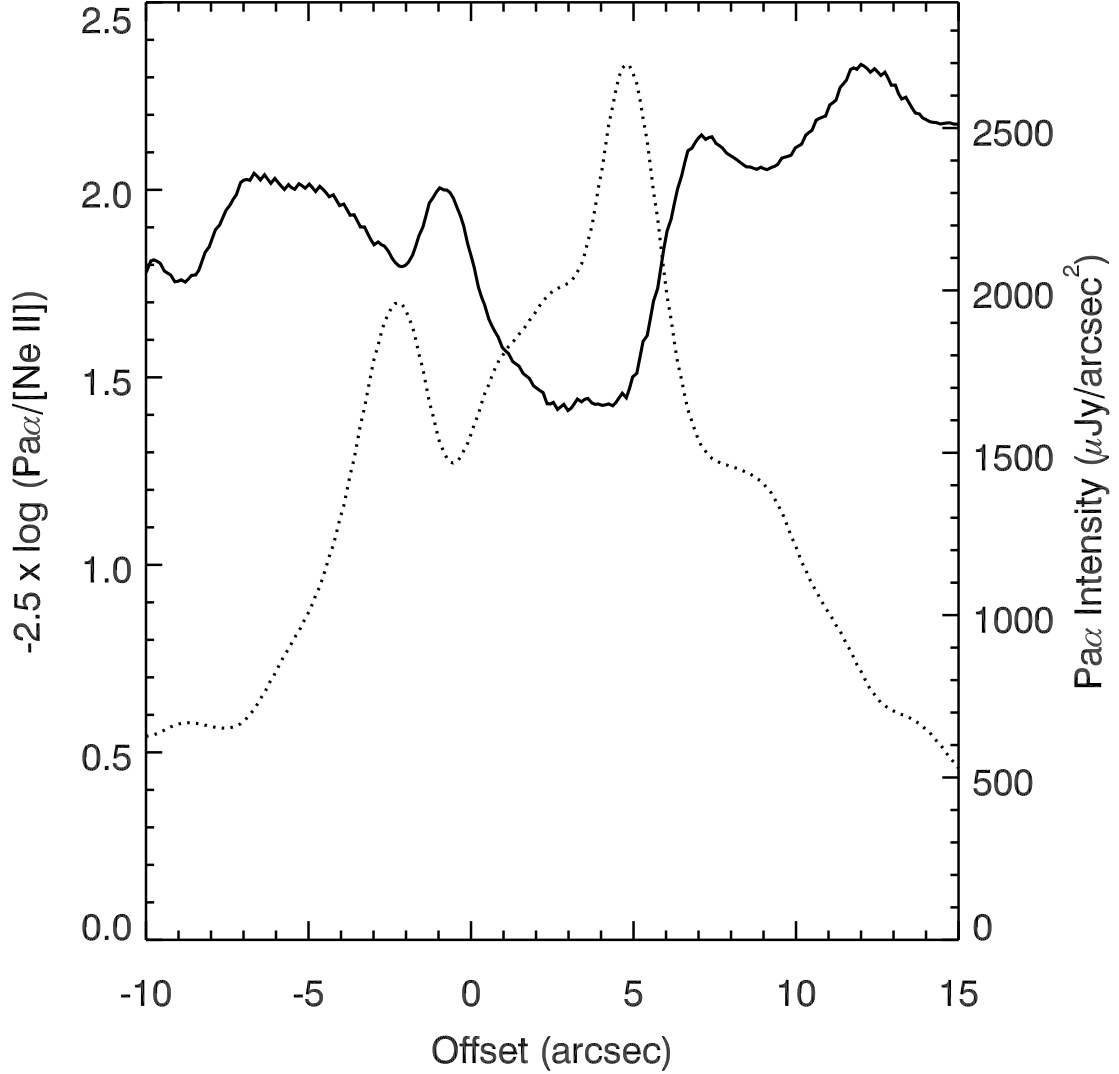


Fig. 3.— The intensity ratio (solid line) of Paschen- α line (in units of $2 \times 10^4 \mu\text{Jy}/\text{arcsec}^2$) to [Ne II] line (in units of $\text{erg s}^{-1} \text{cm}^{-2} \text{sr}^{-1}$) as a function of the offset along the cut perpendicular to the symmetry axis of the H1 (the yellow dashed line on the left of Fig 1). The dashed line is the integrated intensity distribution of the Paschen- α line, convolved with a Gaussian kernel of $1.4''$. The positive offset is toward the southwest.

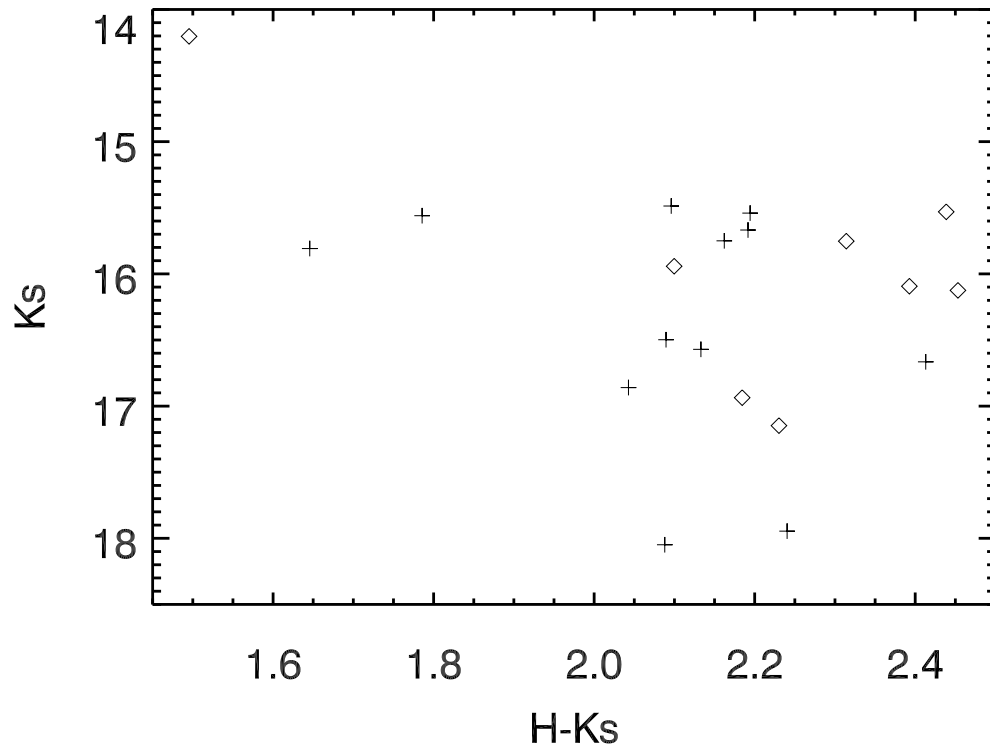


Fig. 4.— In this CMD ($H-K_s$ vs K_s), the plus and diamond symbols represent the stars detected from the *VLT/HAWKI* survey within $2''$ of the western and eastern parts of the northern rim in H1.

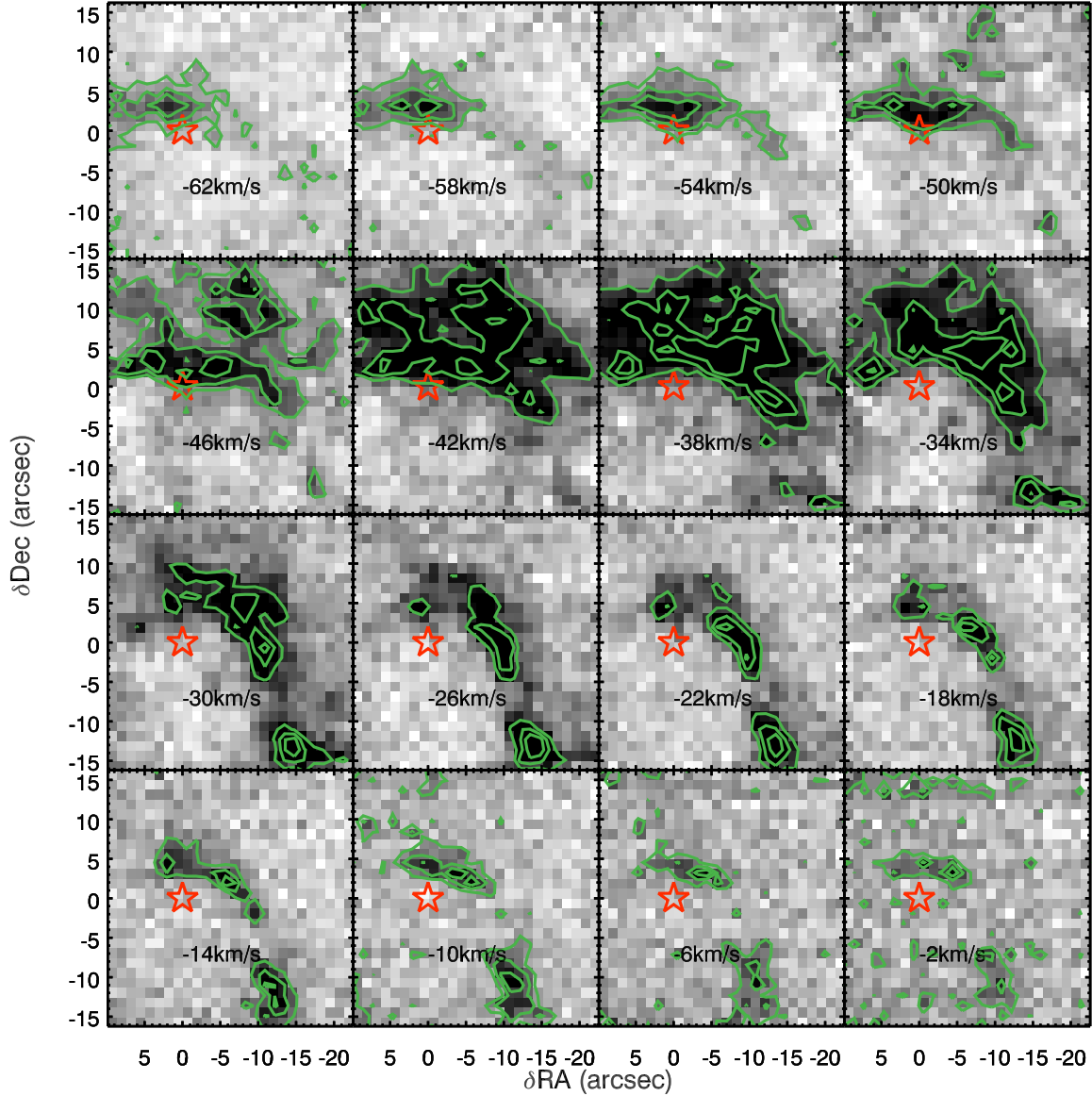


Fig. 5.— Channel maps of the [Ne II] line surface brightness of H1, with the coordinates relative to P114. The velocity is relative to the local standard of rest. The velocity width of each map is 4 km s^{-1} . Green contour levels are at 80%, 60% and 40% of the peak value of the surface brightness, i.e. $0.59 \text{ erg s}^{-1} \text{ cm}^{-2} \text{ sr}^{-1} (\text{cm}^{-1})^{-1}$.

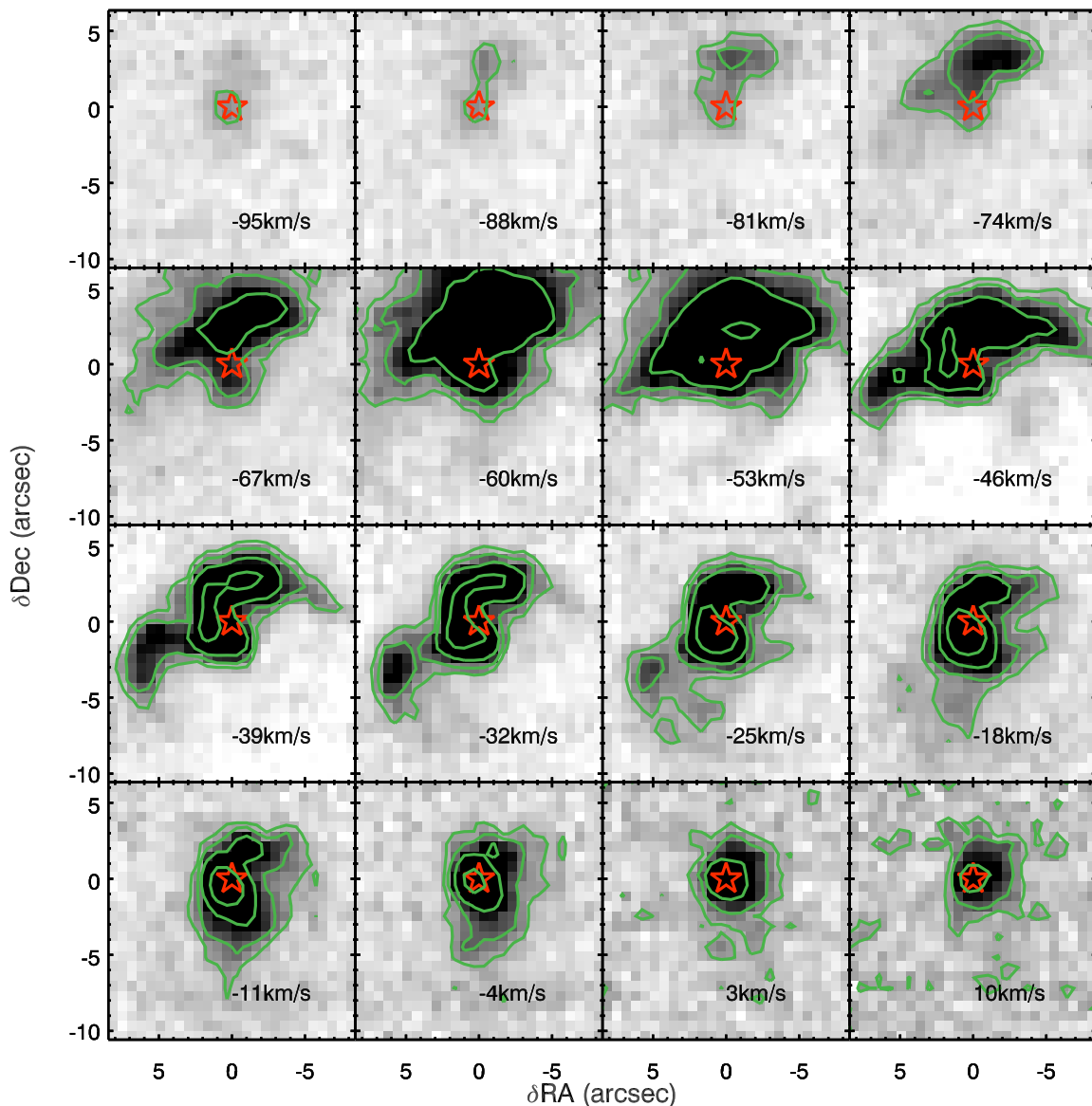


Fig. 6.— Channel maps of the [Ne II] line surface brightness of H₂, with the coordinates relative to P35. The velocity is relative to the local standard of rest. The velocity width of each map is 7 km s⁻¹. Green contour levels are at 30%, 10%, 5% and 3% of the peak value of the surface brightness, i.e. 3.66 erg s⁻¹ cm⁻² sr⁻¹ (cm⁻¹)⁻¹.

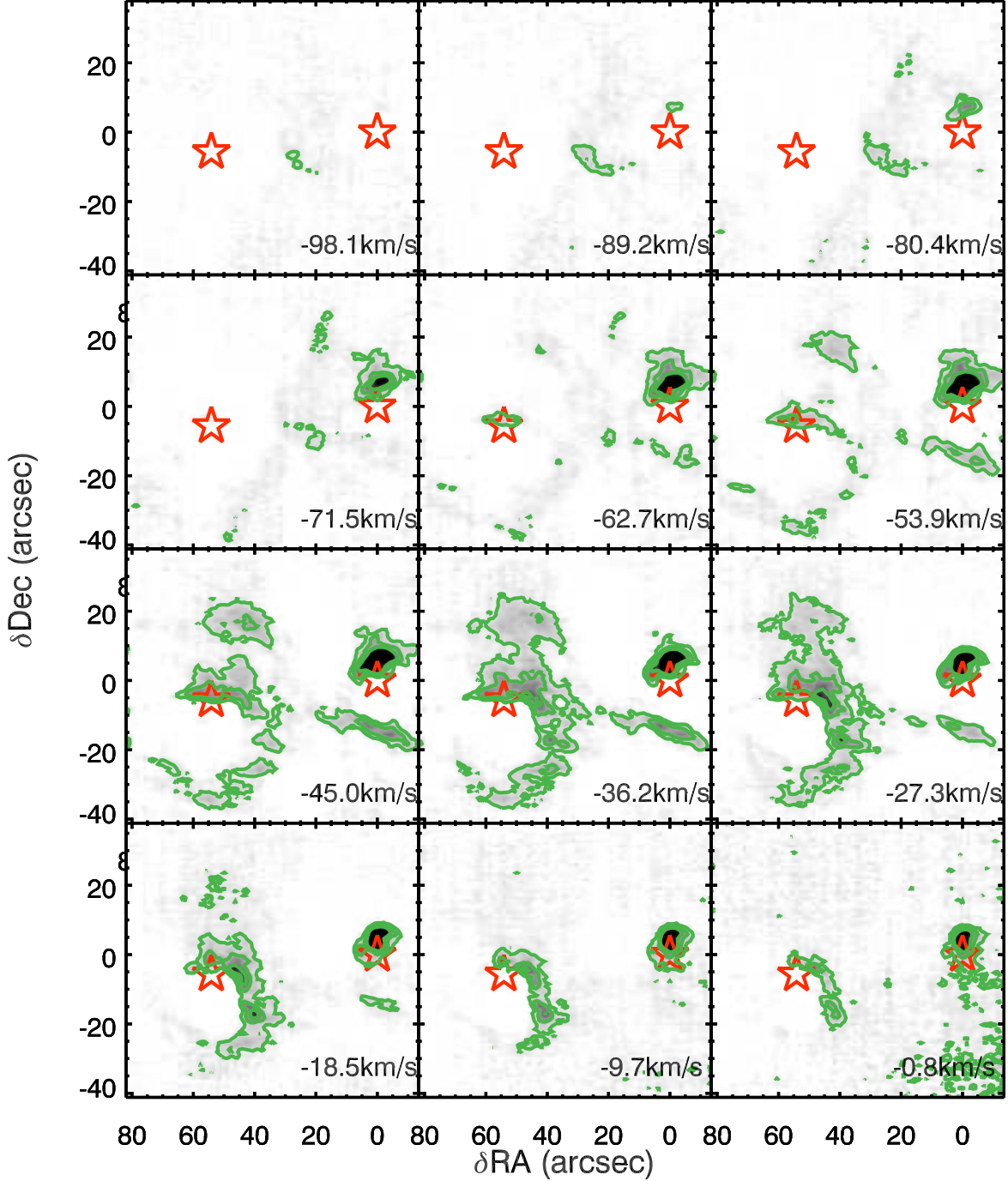


Fig. 7.— Channel maps of the [Ne II] line surface brightness derived from the med-resolution observation. with the coordinates relative to P35. The field-of-view of these images is the same as that of Fig. 1. The velocity is relative to the local standard of rest. The velocity width of each map is 8.84 km s^{-1} . Green contour levels are at 10%, 5% and 2% of the peak value of the surface brightness, i.e. $1.76 \text{ erg s}^{-1} \text{ cm}^{-2} \text{ sr}^{-1} (\text{cm}^{-1})^{-1}$. The two red stars represent the evolved massive stars, P114 and P35 embedded in H1 and H2, respectively.

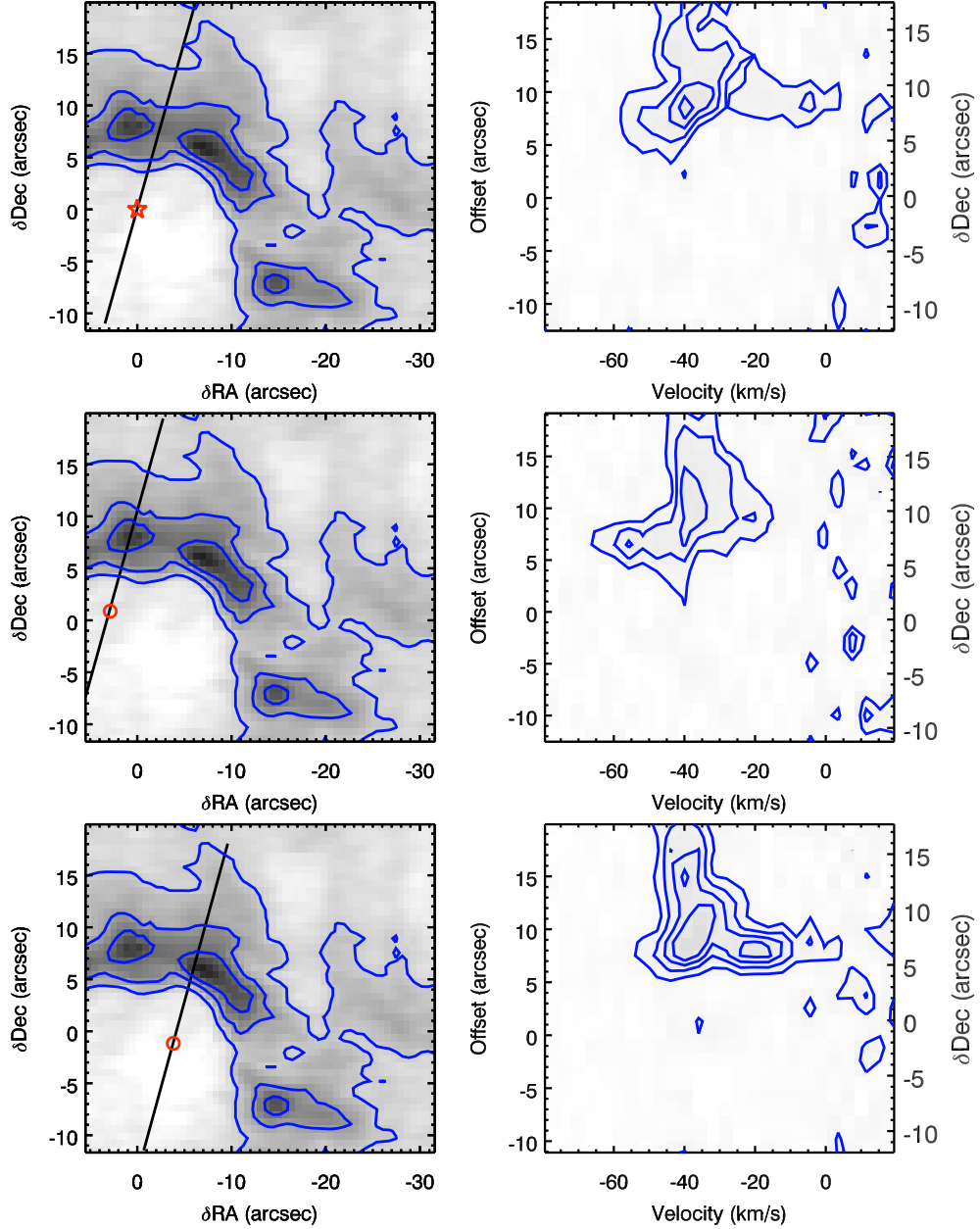


Fig. 8.— Left: TEXES [Ne II] integrated line flux map of H1. The black lines show the cut for the PV diagram on the right. The star and circles are the zero offsets along the cuts. The star also marks the location of P114. The locations along the cut above (below) the star or circles have positive (negative) offsets. Blue contour levels are at 70%, 50% and 30% of the peak value of the integrated line flux map of H1, $0.1 \text{ ergs cm}^{-2} \text{ s}^{-1} \text{ sr}^{-1}$. Right: The PV diagram of the H1 along the cuts parallel to the symmetry axis. Blue contours are drawn at 50%, 40%, 30%, and 20% of the peak value of the surface brightness of H1, i.e. $0.59 \text{ erg s}^{-1} \text{ cm}^{-2} \text{ sr}^{-1} (\text{cm}^{-1})^{-1}$. In the first panel, the cut passes P114, while in the second and third panels, the cuts are in the $3''$ northeast (top left) and $4''$ southwest (low right) away from

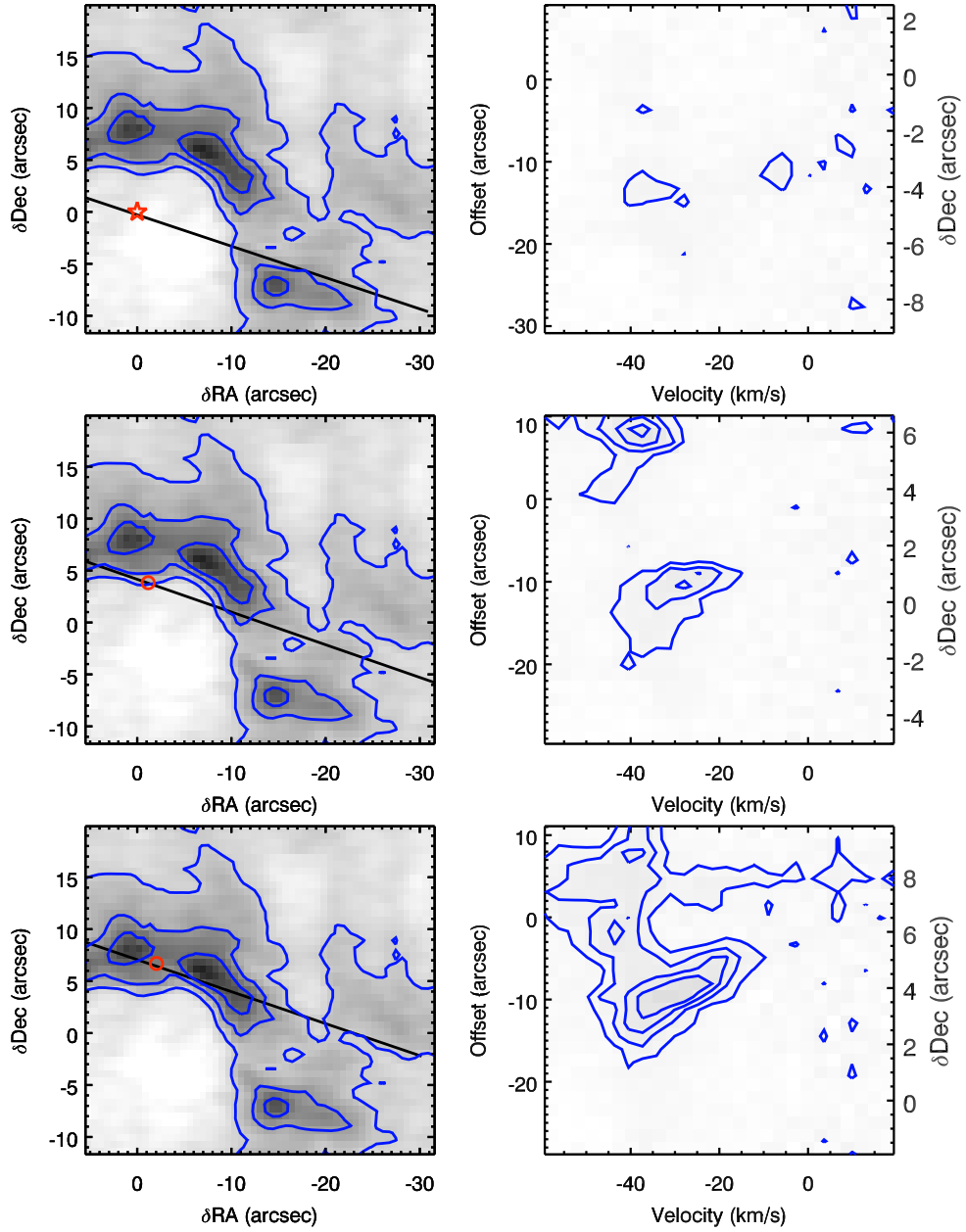


Fig. 9.— The same as Fig.8 except for the cut perpendicular to the symmetry axis. In the second and third panels, the cuts are in the 4'' and 7'' northwest (top right) away from the cut in the first panel.

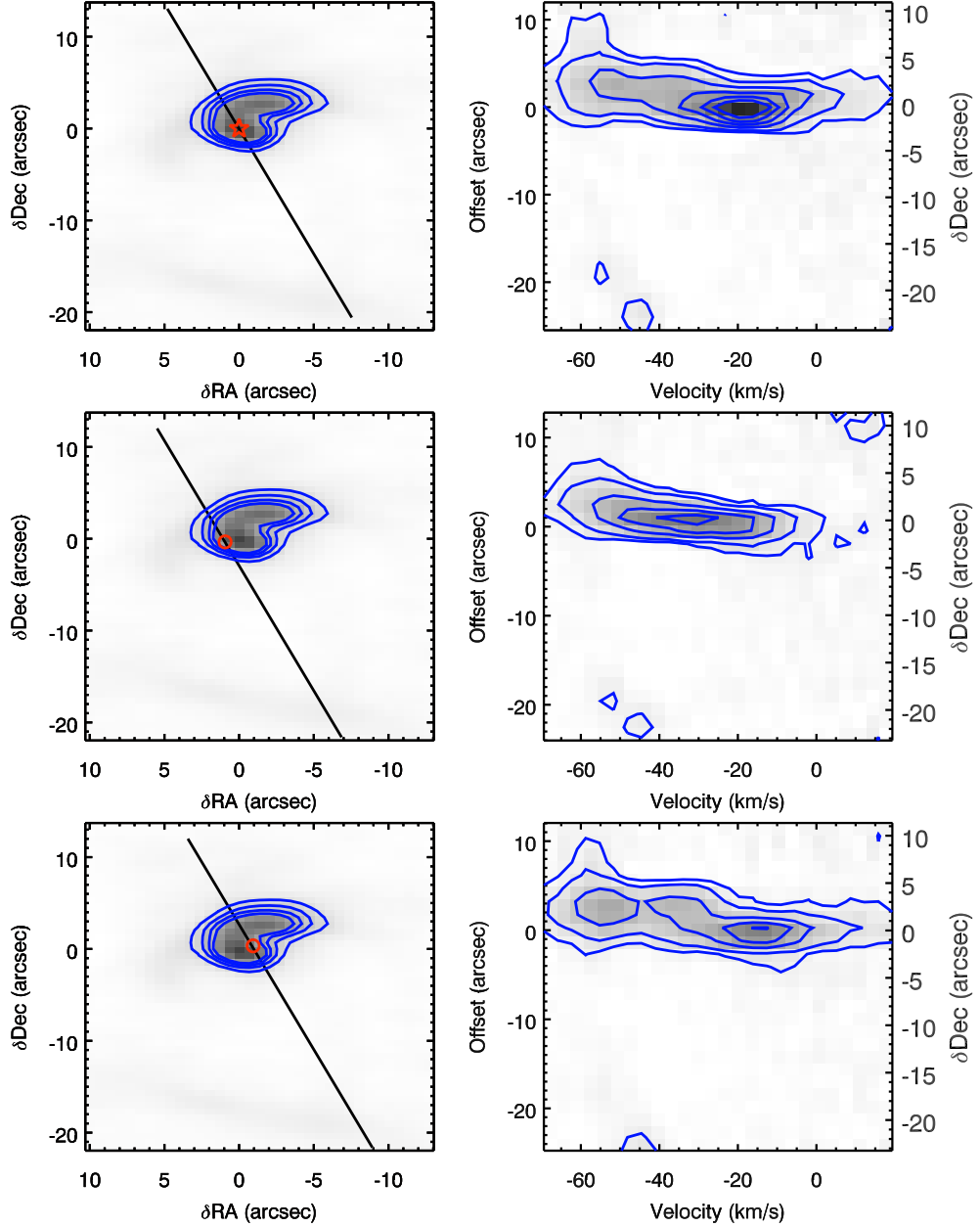


Fig. 10.— The same as Fig.8 except for H₂. For the left panel, blue contours are drawn at 50%, 40%, 30%, and 20% of the peak value of the integrated line flux map of H₂, $0.67 \text{ erg s}^{-1} \text{ cm}^{-2} \text{ sr}^{-1}$. For the right panel, blue contours are drawn at 50%, 40%, 30%, 20%, 10% and 5% of the peak value of the surface brightness of H₂, i.e. $3.66 \text{ erg s}^{-1} \text{ cm}^{-2} \text{ sr}^{-1} (\text{cm}^{-1})^{-1}$. In the second and third panels, the cuts are in the 1'' southeast (low left) and 1'' northwest (top right) away from the cut in the first panel.

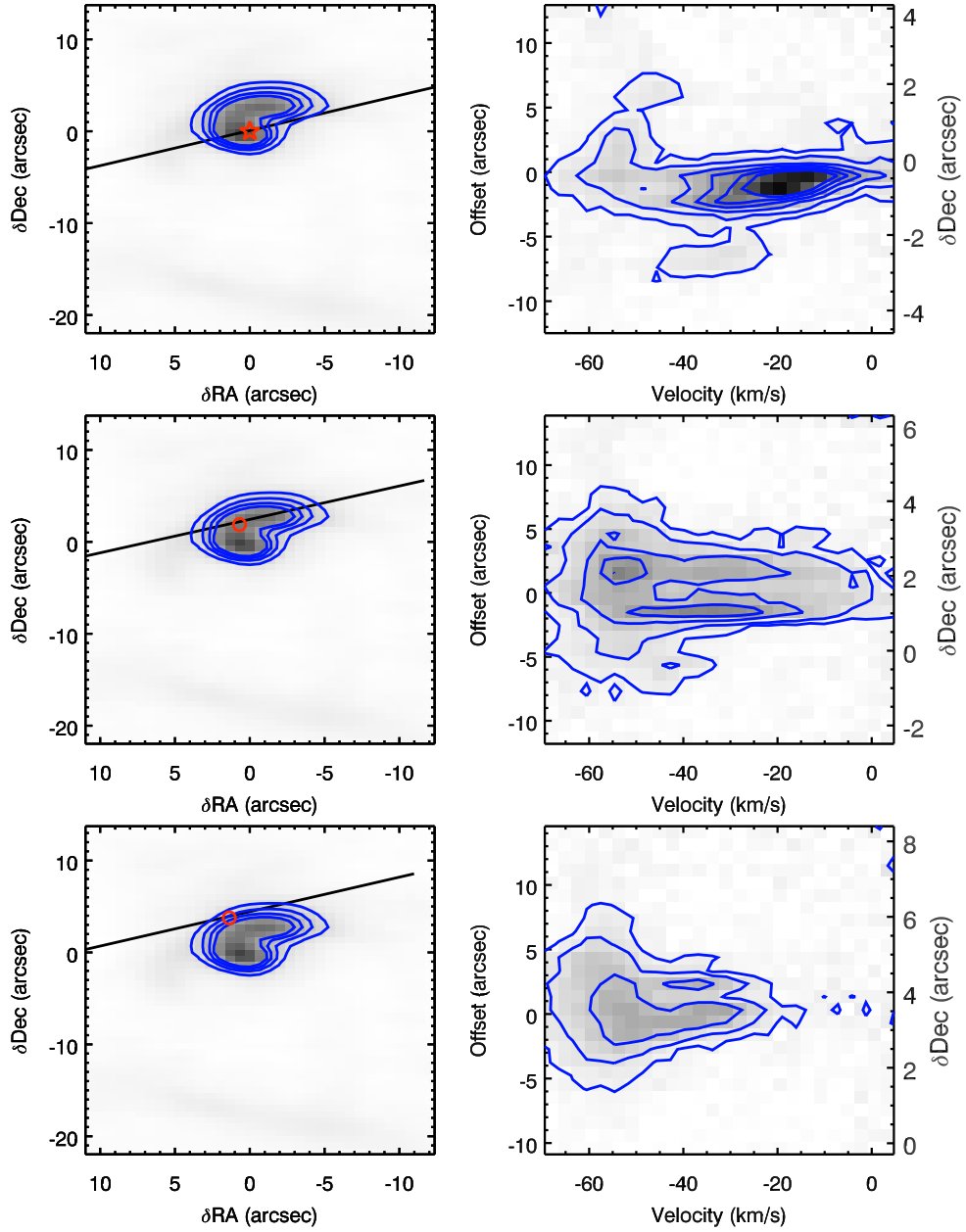


Fig. 11.— The same as Figure 10 except for the cut perpendicular to the symmetry axis. In the second and third panels, the cuts are in the $2''$ and $4''$ northeast (top left) away from the cut in the first panel.

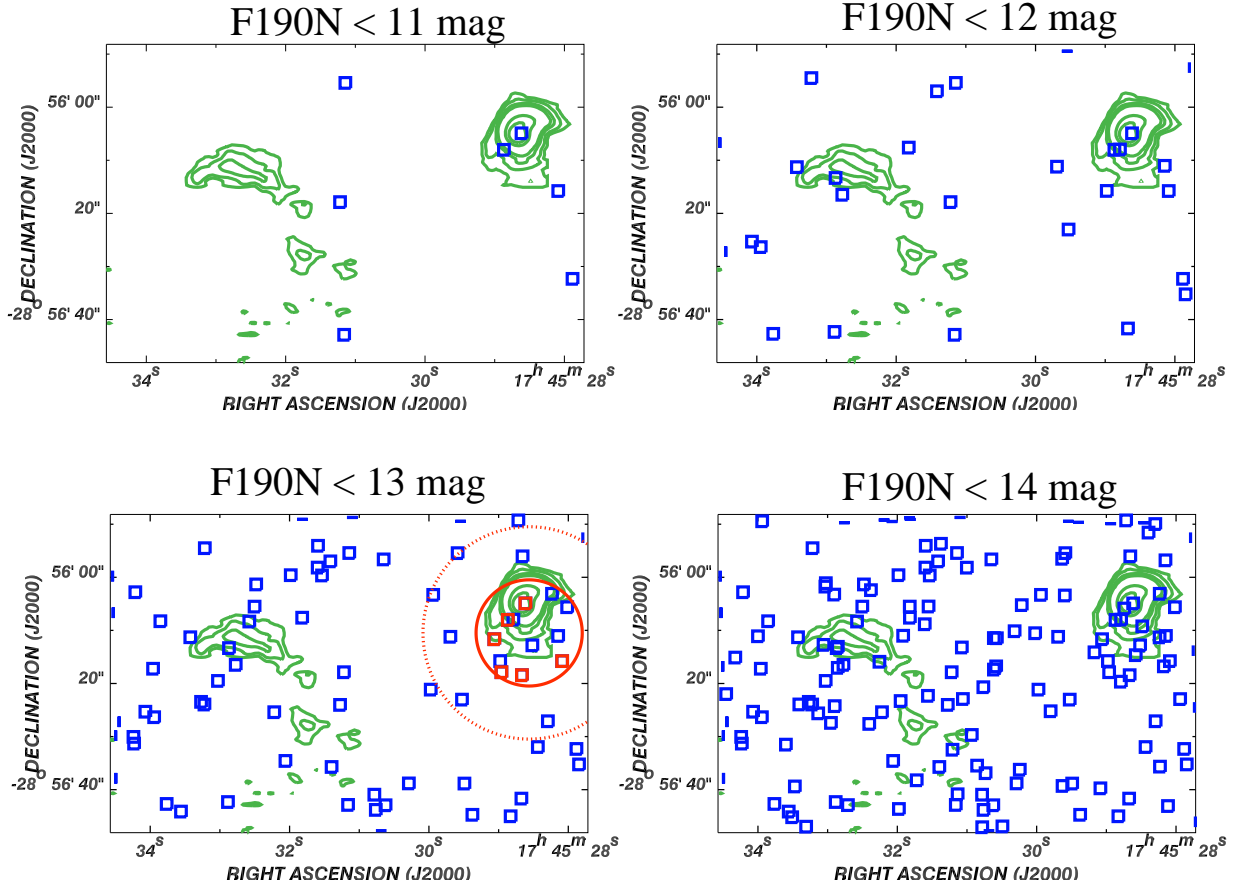


Fig. 12.— The spatial distributions of stars (squares) brighter than the magnitude, as labeled at the top of each panel. The field-of-view of these images and the green contours are the same as those of Fig. 1. The solid and dashed red circles in the lower left panel mark the regions of 10'' and 20'' radii centered on H2. Six stars, colored in red within the 10'' radius have $H-K_s$ colors, similar to P35 (see Fig. 13).

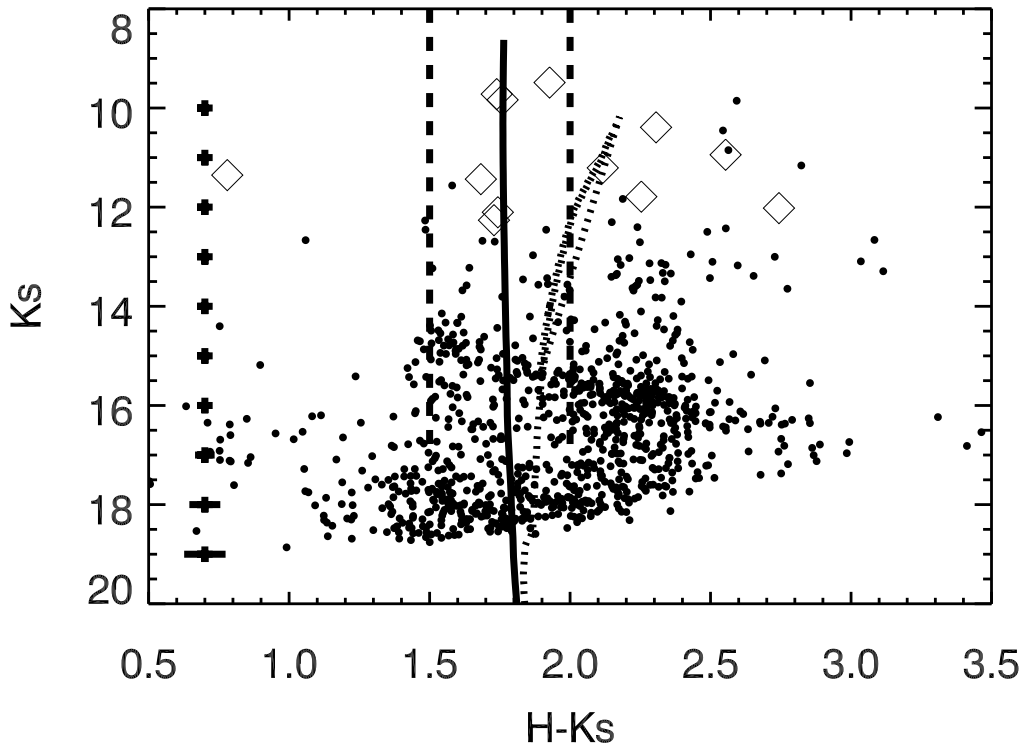


Fig. 13.— The CMD of the stars with available *VLT*/*HAWKI* magnitudes in the central 20'' of H2. Those 12 stars with F190N magnitudes brighter 13 within the central 10'' are marked as diamonds. The error bars (heavy black crosses on the left side) show typical uncertainties in K_s and $H-K_s$. The solid and the dotted lines represent the 2 Myr old Genova and 5 Gyr old Padova isochrones with solar metallicity, respectively. The two vertical dashed lines enclose the color range, which we use to select the six stars (red squares in the lower right panel of Fig. 12) with $H-K_s$ similar to P35.

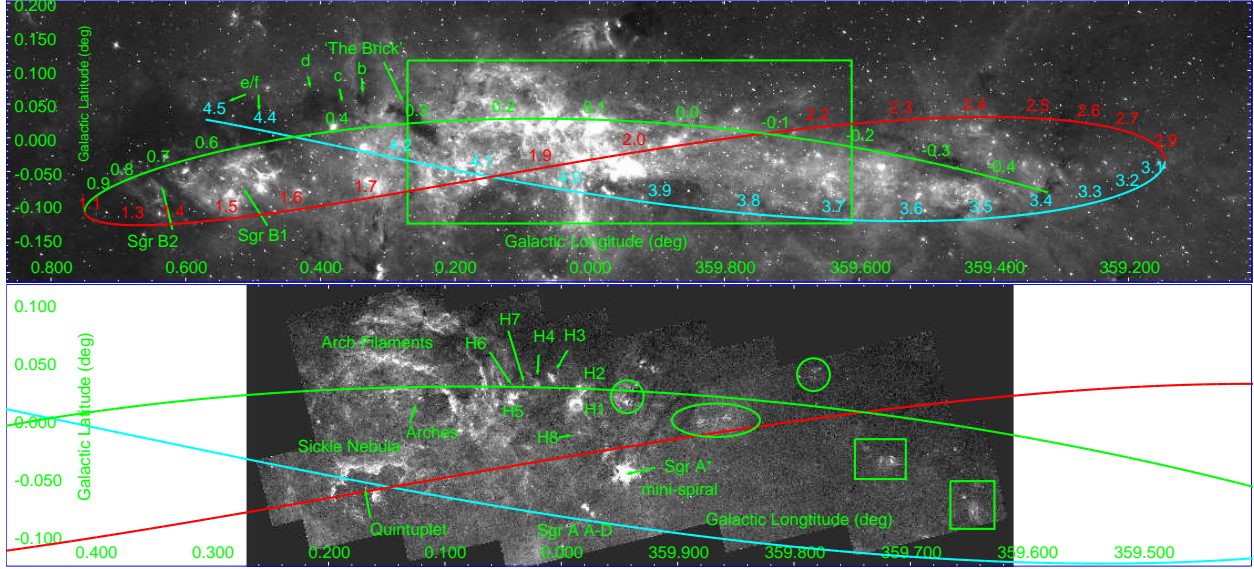


Fig. 14.— The hypothetical orbit of various molecular clouds in the CMZ, as proposed by Kruijssen et al. (2015), overlaid on the *Spitzer*/IRAC $8.0 \mu\text{m}$ (top) and *HST*/NICMOS Paschen- α images (bottom). The green box in the top panel outlines the field-of-view of the Paschen- α image. The numbers marked above the orbit in the top panel indicates how long individual molecular clouds have passed by Sgr A* in the pericentre (the point closest to Sgr A*) near the ‘Brick’ (There are three pericentre in the orbit of molecular clouds given in Kruijssen et al. (2015)); the minus symbol means the time before the passage. Several molecular clouds and two star formation regions, Sgr B1 and Sgr B2, have been marked in the top panel. In the bottom panel, H II regions in the GC are labeled, such as H1-8 (Yusef-Zadeh & Morris 1987). In addition, new H II regions, identified from our *HST*/NICMOS Paschen- α survey are outlined in an ellipse, two circles and boxes.